VascX Models: Model Ensembles for Retinal Vascular Analysis from Color Fundus Images

Jose Vargas Quiros, None^{1,2}, Bart Liefers, None^{1,2}, Karin van Garderen, None^{1,2}, Jeroen Vermeulen, None^{1,2}, Eyened Reading Center, None^{1,2}, Sinergia Consortium, None^{1,5,6,7}, and Caroline Klaver, None^{1,2,3,4}

Keywords: vascx, vascular biomarkers, vascular features, medical image analysis, fundus segmentation, artery-vein segmentation, optic disc segmentation, fovea detection

INTRODUCTION

Interest in measuring retinal calibers dates back to the 1970s when Parr and Spears published their approach to approximate the caliber of the central retinal artery and vein using the calibers of their largest branches [40]. Since the late 1990s, various semi-automatic methods have been developed to perform these calculations with different levels of human and machine involvement, enhancing the efficiency of such measurements [25]. Among these developments were prominent tools such as SIVA (Singapore I Vessel Assessment) [54, 30, 28, 52, 10], IVAN [7, 8], and VAMPIRE (Vascular Assessment and Measurement Platform for Images of the Retina) [41, 47, 48].

Today the understanding of retinal vasculature and its association with diseases has expanded substantially. A significant focus has been placed on biomarkers such as retinal calibers, tortuosity, and branching characteristics. These biomarkers are now studied not only in relation to ocular diseases but also to systemic conditions, particularly cardiovascular diseases [53, 34, 24]. More recently, attention has turned to the retina as a window into brain pathology, with studies linking retinal vascular changes to neurodegenerative diseases such as Alzheimer's disease [17]. Previous work has shown that automatically extracted vascular features improve the performance of diabetic retinopathy (DR) detection and classification [2].

Parallel to the scientific advances, deep learning brought about ground-breaking improvements in segmentation quality across a variety of tasks [27]. This triggered the development of multiple datasets, deep learning architectures and models for the segmentation of the main anatomical structures visible in CFIs: vessel segmentation [32, 35], artery-vein segmentation [19, 15], and disc segmentation. The task of assessing fundus image quality has also received attention Fu et al. [18], Abramovich et al. [1], Gonçalves et al. [21]. More recent are efforts to integrate these models into pipelines for fully automated, explainable, vascular feature extraction. Automorph is the most notable example of an open source deep-learning-based pipeline integrating vessel segmentation, artery-vein segmentation, disc segmentation, and vascular feature extraction Zhou et al. [57]. Automorph has been applied in various studies including on the reproducibility of its features [50, 51, 20, 11]. The availability of disc segmentation models in Automorph allows for region-based analysis which isolate features from specific areas of the retina.

Despite these developments, the robust segmentation of retinal morphology (arteries, veins, optic disc, fovea) from CFIs across a variety of patient and imaging conditions remains unsolved. Most publicly available training datasets for artery-vein segmentation are small and homogeneous, often limited to images from a single device, centered on a single anatomic region (fovea or optic disc), and with a fixed field of view. Until recently [49], the largest publicly available dataset for artery-vein segmentation contained only 45 images [4]. Additionally, the pathology and demographics of the study population are often restricted, which significantly impacts the

¹Department of Ophthalmology, Erasmus University Medical Center, Rotterdam, the Netherlands

²Department of Epidemiology, Erasmus University Medical Center, Rotterdam, the Netherlands

³Department of Ophthalmology, Radboud University Medical Center, Nijmegen, the Netherlands

⁴Institute of Molecular and Clinical Ophthalmology, University of Basel, Switzerland

⁵Department of Computational Biology, University of Lausanne, Lausanne, Switzerland

⁶Jules Gonin Eye Hospital (HOP), Fondation Asile des aveugles, Lausanne, Switzerland

⁷Department of Clinical Neuroscience, Laussane University Hospital, Laussane, Switzerland

generalizability of the models trained on these datasets. This affects the downstream extraction of explainable vascular features, which depend on the quality of such segmentations [45, 11]. This is particularly problematic in analyses of large cohort studies and clinical data, which may encompass a diverse range of devices and capture conditions. To overcome these drawbacks, larger and more diverse training datasets are needed to develop models that work reliably across a broader spectrum of conditions.

In this paper, we present contributions towards a robust analysis of the retinal vasculature through improved segmentation and localization models. Our contributions are the following:

- We present models for optic disc, vessel, and artery-vein segmentation and fovea localization, fundamental
 models in the development of CFI analysis systems, especially of the retinal vasculature. We built our
 models using public datasets and new annotations by professional graders on diverse sets of CFIs from
 Dutch studies, mainly the Rotterdam Study.
- We benchmark our models against publicly available models [57, 19] and show significant improvements in segmentation performance. We characterize the performance of the models with respect to image quality as measured using our quality assessment model.
- We evaluate the quality of features extracted from model output by comparing them to features extracted from segmentations made by experienced graders.
- We publicly release and make open-source our pre-processing and inference code, including model weights.

METHODS

Datasets

We trained and evaluated our models on a combination of public datasets and images from the Rotterdam Study (RS) and other Dutch studies.

Public Datasets

We collected publicly available datasets from previous work. These datasets have different patient demographics, pathologies, retinal regions (fovea and disc centered), field of view and countries of origin. Table 1 shows an overview of these datasets. For complimentary details including capture devices and resolution see Supplementary Table 4.

We included several well-known vessel and artery-vein segmentation datasets with diabetic retinopathy (DR) patients [23, 4, 36, 6]. We excluded the DRIVE dataset [46, 43] due to its low resolution (584 × 565 pixels). We included the larger and more recent FIVES [29] and Leuven-Haifa [49] datasets, which contain a mixture of diseased and healthy patients. On the other hand, most datasets with disc segmentations were originally collected for the assessment of glaucoma Zhang et al. [56], Kovalyk et al. [31], Fang et al. [14]. The REFUGE2 dataset, an extension of the original REFUGE dataset Orlando et al. [38] is notable for its size (2000 CFIs), various anatomic regions captured, and for containing fovea location annotations. We also included ADAM (age-related macular degeneration) [13], PALM (pathological myopia) [12] and IDRiD (diabetic retinopathy) [42]; which also contain fovea positions.

Finally, we used the Eye-Quality (EyeQ) dataset (Table 1) for the quality estimation algorithm. This dataset contains manual gradings of fundus quality from 28,792 images using a 3-class system. CFIs were graded as one of: unusable/bad, usable and good quality. It is unique for its size and for containing a variety of capture devices and image conditions. The field-of-view of the images in our training set is between 30° and 50°, which includes the vast majority of standard fundus imaging devices.

Rotterdam Datasets

We complimented the CFIs from the public data sets with images available to the Department of Ophthalmology at Erasmus Medical Center in Rotterdam; mainly the Rotterdam Study (RS). The RS is a prospective population-based cohort study of people living in Ommoord, a district of the city of Rotterdam (Ikram et al. [26]). The RS consists of four cohorts, all of which were used in this work. The minimum age of study participants varies between > 55 in the first cohort and > 40 in the fourth. Each cohort was followed for multiple rounds of follow-up examinations every 4 to 5 years. Most of the visits in the RS involved the capture of CFIs on both eyes. Due to the multi-decade span of the RS, multiple devices, capture conditions and fields (macula and disc centered) are present in the dataset.

Table 1. Overview of datasets for various segmentation and localization tasks. Pathologies: H: healthy, GC - glaucoma (all types), NTG: normal tension glaucoma, HTG: high tension glaucoma, HT: hypertension, DR: diabetic retinopathy, AMD: age-related macular degeneration, PM: pathological myopia, O: other eye diseases. *: 379 of 1200 samples were discarded due to containing no disc segmentation for partially visible discs. †: 21 of 1200 CFIs were discarded due to having no associated annotation.

Dataset	N	Origin	Ages	Pathology	Region	FOV
			Vessel Segme	entation		
Chase DB [16]	28	UK	Children		OD	35°
DRHAGIS [23]	40	UK	NR	10 GC, 10 HT, 10 DR, 10 AMD	M	45°
HRF [4]	45	GER	NR	15 H, 15 DR, 15 GC	M	45°
RETA [36]	54	IND	NR	Signs of DR	M	50°
FIVES [29]	800	CN	4-83	H, GC, DR, AMD	M	50°
Leuven-Haifa [49]	240	BE	18-90	75 NTG, 63 HTG, 56H, 30 O	OD	30°
Rotterdam (ours)	352	NL	40+	See Fig	ure 1.	
Total	1559					
		د	Artery Vein Seg	mentation		
RITE [43]	40	NL	25-90	7 DR, 33 no DR	M	45°
HRF-AV [6]	45	GER	NR	15 H, 15 DR, 15 GC	M	45°
Les-AV [37]	22	NR	NR	NR	OD	30°
Leuven-Haifa [49]	240	BE	18-90	75 NTG, 63 HTG, 56H, 30 O	OD	30°
Rotterdam (ours)	215	NL	40+	See Fig	ure 1.	
Total	562					
			Disc Segmen	ntation		
ORIGA [56]	650	SGP	40-80	Multiple	OD	NR
PAPILA [31]	488	SPN	15-90	87 GC, 333 H, 68 O	OD	30 °
IDRiD [42]	81	IND	NR	Signs of DR	M	50°
ADAM [13]	821*	CN	53.2 ± 15.6	267 AMD, 933 O	M, OD, MP	45 °
PALM [12]	1179†	CN	37.5 ± 15.91	637 PM, 563 O	M, OD, MP	45 °
REFUGE2 [14]	2000	CN	NR	280 GC, 1720 H/O	M, OD, MP	45 °
Rotterdam (ours)	1225	NL	40+	See Fig	ure 1.	
Total	7464					
			Fovea Local	ization		
IDRiD [42]	516	IND	NR	Signs of DR	M	50°
ADAM [13]	1200	CN	53.2 ± 15.6	267 AMD, 933 O	M, OD, MP	45 °
PALM [12]	1200	CN	37.5 ± 15.91	637 PM, 563 O	M, OD, MP	45 °
REFUGE2 [14]	2000	CN	NR	280 GC, 1720 H/O	M, OD, MP	45 °
Rotterdam (ours)	10908	NL	40+	See Fig		
Total	15824					
CFI	Quality Es	stimation				
EyeQ [18]	28,792					

In addition to the RS, we included images captured during the Randomized Controlled Trial for Age-Related Macular Degeneration (AMD-Life) [9]; which consisted of 150 patients aged 55–85 years imaged with a Topcon 3D OCT 2000-plus and Topcon TRC-50EX cameras. Images from the Dutch Myopia Study (MYST) [22] which included younger subjects (mean (SD) age of 47.3 (12.9) years) were also used. These images were captured with a Topcon TRC-50EX.

CFI Selection and Weighing

We used most public datasets in their entirety without filtering, after harmonizing annotations when necessary. The main exception were disc segmentations in the ADAM dataset, where 379 of 1200 samples were discarded due to containing no disc segmentation for partially visible discs.

Regarding the Rotterdam sets, we sampled CFIs at random from all available images. We included fundus images captured by OCT machines to improve diversity of devices in the dataset. For the vessel and A/V segmentation datasets (Table 1), due to the much larger size of the Rotterdam Study compared to AMD-Life and MYST, we over-sampled CFIs from these sets to make up 15% of the samples. We used the quality estimation model in Automorph [57] to assess image quality and excluded images classified as *unusable*. Additionally, we asked graders to exclude images for which they found the quality to be unusable for the task at hand.

For disc segmentation, due to the large size of publicly available datasets (Table 1), we first used a model trained on publicly available datasets to automatically identify failure or challenging CFIs. We selected CFIs for which no disc was detected or a disconnected disc mask was produced by the model. A trained grader reviewed these images and identified the ones where the disc was present but incorrectly segmented, and these were included in the training set. In practice, these included many analog, macula-centered images from the Rotterdam sets, which specially challenged the model.

For fovea detection, we used CFIs from a sub-cohort of the RS previously graded for signs of Age-related Macular Degeneration (AMD); which included localization of the fovea for ETDRS grid placement.

Figure 1 shows the statistics of the final Rotterdam development sets. Vessel and artery-vein segmentation sets are similar (partly due to overlap) and are closer to the overall distribution of the RS. The disc segmentation dataset, on the other hand, contains more images from the analog devices, which were often the hardest to segment partly due to unconventional disc placement.

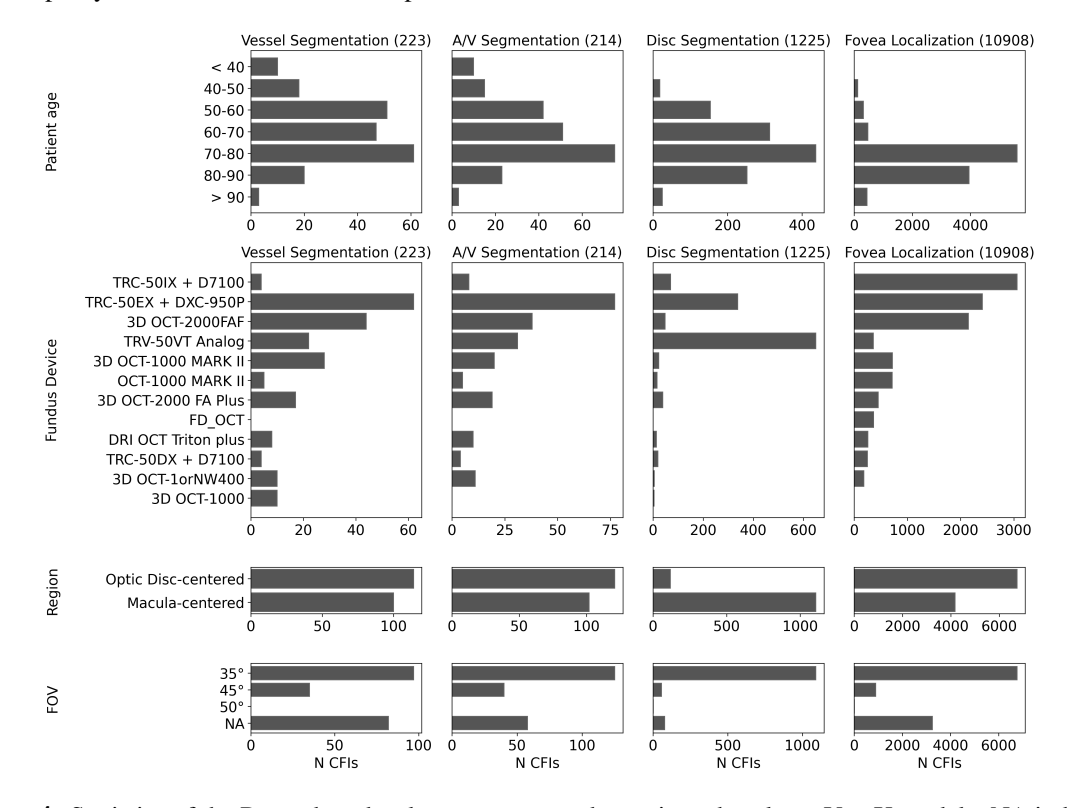


Figure 1. Statistics of the Rotterdam development sets used to train and evaluate VascX models. NA indicates the information was not available.

CFI annotation

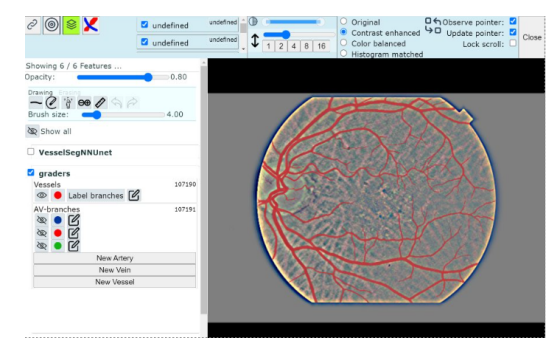
Images were annotated using custom software for ophthalmological image annotation [33]. Four professional graders participated in the process. The graders worked on desktop computers with a drawing tablet for segmentation. The annotation process was different per annotation type:

Vessel segmentation We followed an AI-assisted process by initializing the drawing interface with with outputs from vessel segmentation models. Initially (first 200 images) we made use of models trained on public data (including Automorph Zhou et al. [57]) to later switch to a model trained on both public data and annotations from previous iterations of this process. The graders were instructed to independently fix the masks produced by the model, including missing vessels and over-segmentation. A digitally enhanced version of the image with increased contrast of vessel edges was used to aid the graders (Figure 2a).

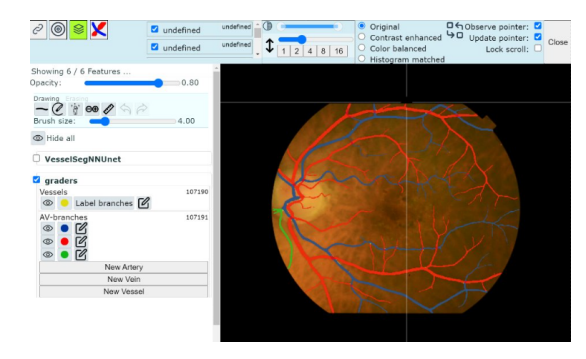
Artery-vein segmentation We resolved connectivity issues at artery-vein crossings by annotating arteries and veins on separate layers. An interface was developed specifically for artery-vein segmentation (Figure 2b) to allow the graders to start from a vessel segmentation (no A/V distinction) and color arteries and veins into two independent masks or layers using drawing tools. A third layer - *Unknown* was added for vessels that could not be recognized as either. They were asked to color A/V crossings on both layers (overlapping). They were able to visualize and correct each layer independently, or all the same time. Another feature allowed them to visualize the connected components of each mask in different colors to easily find mistakes in connectivity. The entire process consisted in 1) correcting mistakes in the provided mask (vessel segmentation); 2) coloring the mask into A/V and unknown colors/layers; 3) Verifying connected components on the A/V masks and filling any gaps.

Disc segmentation A single professional grader performed this annotation using the same drawing interface used for binary vessel segmentation (Figure 2a). The grader colored the entire optic disc area excluding any peri-papillary atrophy (PPA) region to match the annotations on public datasets [3, 56, 14]. In cases of doubt due to poor image quality or unclear disc boundaries, a consensus was reached between the three graders. Cases where the image quality was too poor to reach consensus were excluded.

Fovea localization The fovea was localized by four graders who followed a standard grading protocol which included placing an ETDRS grid; overlaid on the images.



(a) Vessel segmentation: graders corrected binary masks generated by AI, using a digitally contrast-enhanced image to visualize vessels.



(b) Artery-vein segmentation: graders colored the vessel masks into two separate (overlapping) masks for arteries and veins using a custom interface.

Figure 2. Screen capture of the software used for all the annotations on Rotterdam CFIs.

Model Training

We implemented an improved CFI bounds detection and pre-processing procedure and used well-known model architectures such as U-Net for model training.

Data Pre-processing

For all models, training and testing CFIs were pre-processed via:

1. Detection of the CFI boundaries defined by a circle and top, bottom, left and right lines (see Figure 3).

- 2. Cropping of the CFI along its boundaries into a square image and resizing to 1024x1024px.
- 3. Contrast enhancement via Gaussian filtering. The image was mirrored along its boundaries before contrast enhancement to avoid artifacts, and the region outside its boundaries was blacked out after enhancement.

The geometric steps (cropping and resizing) were replicated on the labels for training. Figure 3 shows outputs of our pre-processing algorithm. Models were trained on the concatenation of the cropped CFI and its contrast-enhanced version (6 input channels).

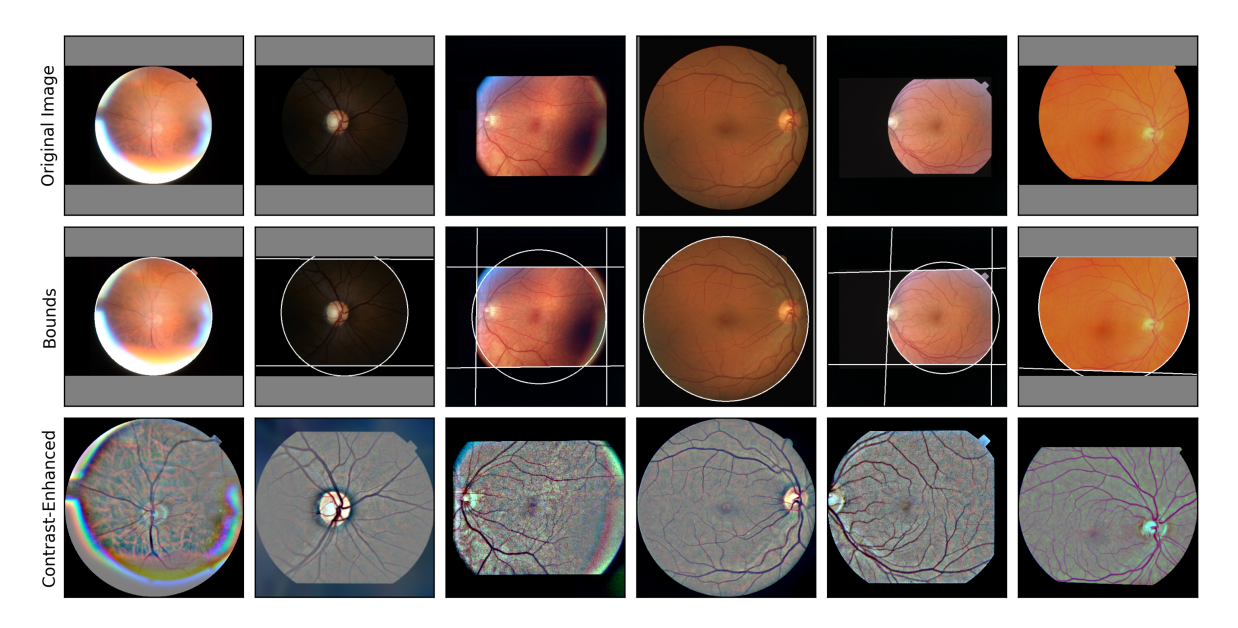


Figure 3. Sample of pre-processed images from the Rotterdam sets, showing: original images (first row), the results of bounds detection defined by the intersection of a circle and optional lines (second row) and the cropped and contrast-enhanced image (third row).

Vessel, A/V and Disc Segmentation Models

Vessel and A/V segmentation models were trained separately given the different development sets. Data was augmented via random appearance transforms: de-focus, hue-saturation-value, Gamma and Gaussian noise; followed by geometric transforms: flipping (horizontal and vertical), random scale (1.0-1.15 times original scale) random rotation (up to 10 degrees), random elastic transforms and finally random cropping of a 512x512px patch. This was done to maintain enough resolution for the segmentation of the thinner vessels. Correspondingly, inference is done on 1024x1024px images via a sliding window with 50% overlap. A Gaussian kernel was used for merging window segmentations. Test-time augmentation was also applied: the outputs of horizontal, vertical, and horizontal-vertical flips were averaged together before binarizing the final output. These procedures closely follow or are inspired by the process followed in NN-Unet Isensee et al. [27].

Vessel annotations were encoded as 0) background and 1) vessel. Artery-vein annotations were encoded as 0) background, 1) arteries, 2) veins, and 3) crossings (both artery and vein). We used this approach for A/V segmentation with the goal of boosting the relative importance of the crossings in the loss function. The loss function was the sum of Dice and Cross-entropy with equal weights. The optic disc segmentation model was similarly trained on binary masks encoded as 0) background and 1) disc mask; with the same loss function. Figure 6a shows sample training batches for the vessel and artery-vein segmentation models.

The models were trained making use of a custom implementation of the U-Net with 6 input channels (for original RGB image and contrast-enhanced version), 8 down-sampling stages, and deep supervision (loss calculated on the down-sampled stages too). The input resolution was 512x512px.

Fovea Localization Model

The fovea localization model was trained separately to localize keypoints on the CFIs. A heatmap regression approach [55] with the same U-Net architecture used for artery-vein segmentation as backbone. Heatmap regression consists in training the model to regress a probability image or heatmap of the keypoint location.

The pixel location of the maximum on the output heatmap is then taken as the output keypoint location. Train heatmaps may be generated using different probability density functions centered at the ground truth keypoint location. We generated target heatmaps (512x512px) using a Gaussian with constant σ centered at the keypoint. The value of $\sigma = 50px$ was selected via experiments on a holdout set for the task of localizing the disc center on CFIs. Mean squared error (MSE) was used as loss function to train the model to approximate the continuous target heatmaps. The location (2D-index) of the maximum over the heatmaps output by the model was taken as the keypoint location.

Input CFIs were augmented via random appearance transforms: de-focus, hue-saturation-value, Gamma and Gaussian noise; followed by geometric transforms: horizontal flipping, random scale (1.0-1.05 times original scale) random rotation (up to 5 degrees) and finally resizing down to model input size. Test-time augmentation was correspondingly applied using the vertical flip of the input. Figure 7 shows sample training batches for the disc segmentation and fovea localization models.

Quality Classification Model

The image quality classification model was trained using the same augmentations as for fovea and disc models. The models were developed by fine-tuning Resnet101 (Imagenet weights) with 224px input resolution. Here we used only the original RGB CFI (3 channels; no contrast-enhanced version). All the model weights were fine-tuned (no frozen layers). The cross-entropy loss was used for classification and Mean Squared Error (MSE) for regression. Test-time augmentation was applied by averaging the outputs of the original and horizontally-flipped inputs.

Training Setup

For all models, we made use of the *albumentations* library for data augmentations. Pytorch and *pytorch-lightning* were used to develop our model training pipeline.

Training and evaluation were done via a 5-fold cross-validation loop. Group-fold cross-validation was used to ensure that images of the same eye were always together in either training or test set. The batch size was set to 16 for all models. The Adam optimizer was used with lr = 0.001 for segmentation. Models were trained for a fixed number of epochs across folds: 100 for vessel segmentation; 200 for A/V segmentation; 100 for disc segmentation and 35 for fovea localization. This was decided approximately based on experiments with a partition of 20% of the training set. We observed flat performance progression on these sets before and after the chosen epoch number and did not consider it necessary to do further optimization. Some architectural choices such as the use of deep supervision and increased UNet depth were validated using the same partition.

Per-fold models were trained on a cluster using a single NVidia graphics card per model. Segmentation models were trained in mixed precision.

Evaluation

We evaluated our models via 5-fold cross-validation, with the Dice score as the main evaluation metric. We report the mean scores (separated per source dataset) over the five validation sets. This is to provide a score of generalization performance on all datasets 1. For all models, we input pre-processed images in 1024x1024px resolution. Test-time augmentation was enabled. Note that this evaluation setup means that the scores of our models could be slightly under-represented when compared to the full ensemble of our models.

For the A/V model artery and vein masks were recovered from the model outputs. For the VascX model, this meant merging the *Crossings* output mask with both *Artery* and *Vein* masks.

RESULTS

Comparison with Publicly Available Models

We compared the performance of our models with that of publicly available ones. Note that our goal was not to compare deep learning architectures but instead to compare the performance of entire systems (including architecture, inference code, and public model weights) across different datasets (Table 1). Therefore architectures published without publicly available weights have been excluded from this analysis.

We compared the three segmentation models (vessels, artery-vein, disc) to the models in Automorph [57], the most comparable pipeline that integrates vessel, A/V, and disc segmentation. For each task, we compared against the corresponding model ensemble (7 models) in the Automorph pipeline. Additionally, we compared vessel and A/V models to Little-WNet (LWNet) [19], a dedicated vessel and A/V segmentation model with publicly available weights. The LWNET vessel segmentation weights were trained on DRIVE. For A/V segmentation we

tested both DRIVE and HRF-trained weights. We found DRIVE weights to perform better across all datasets and therefore report only these scores.

Table 2 shows the results of our comparison using Dice score (segmentation) and Euclidean distance (fovea localization) as evaluation metrics, which reveal consistently higher performance from VascX across all datasets. Note that not all model - dataset pairs were evaluated due to the model being trained on the corresponding dataset entirely.

For A/V segmentation VascX achieved higher Dice scores across all datasets, with slightly higher performance for veins than for arteries, as has been observed in previous work [15]. Importantly, we observed large improvements in the Rotterdam and Leuven-Haifa datasets, the only ones evaluated across the three models (Figure 1). The differences was ~ 0.1 for the Rotterdam dataset, the most diverse of the datasets; suggesting increased model robustness.

Regarding disc segmentation, the largest difference was in the Rotterdam dataset, where Automorph achieved a score of only 0.220. Many of these failure cases were due to Automorph's bounds detection algorithm failing on Rotterdam CFIs. The disc detection was however also prone to fail for discs located close to or crossing the bounds of the CFI; and for images for which the disc border had low contrast.

Qualitatively we observed a marked improvement in segmentation performance from VascX models. Figure 4 shows example model outputs from Rotterdam and Leuven-Haifa inputs (the two independent datasets). We observed more consistent disc detection from VascX, especially in cases where the disc was not clearly differentiated. A/V segmentation, while not flawless, produced visibly less continuity and mis-classification mistakes than both LWNet and Automorph. Importantly, many of the vessel crossings were correctly resolved on both artery and vein masks.

Effect of Image Quality

To more deeply characterize the performance of the model, we made use of the CFI quality estimation model to classify Rotterdam images into *Good*, *Usable* and *Bad / Unusable* categories. We limited this analysis to the Rotterdam dataset set due to the other dataset being smaller and/or highly uniform in terms of image quality and capture conditions. Figure 5a displays the distribution of Dice scores over image quality bins, as assessed by the model. Figure 5b shows the Dice score distributions for optic disc and macula-centered images. Once again vessel segmentation models achieved high consistency even for CFIs classified as *bad* quality.

Feature Accuracy

The primary goal of our models is to serve as the backbone for explainable vascular feature/biomarker extraction systems. Therefore we quantified the quality of such features. We compared features extracted from model segmentations (VascX, Automorph (AM) and LittleWNet (LWN)) with reference features extracted from the annotations in our development set, which we considered ground truth. We quantified the quality of model features by measuring mean absolute error (MAE) and correlations with the ground truth features. We used the Rotterdam set as main evaluation set for this comparison due to its diversity and size. Due to our 5-fold cross-validation setup for training, for VascX we made use of segmentations generated within each fold to have independence of the test set. Therefore the performance of our models might be under-estimated when compared to the full ensemble.

We made use of a vascular feature extraction to extract a set of features including tortuosity and central retinal equivalents (CRE) from segmentation masks. See Supplementary Section B.0.1 for feature implementation details. The features are calculated using artery-vein segmentation masks, and some (CREs, temporal angles, vascular density) use disc segmentation masks and fovea locations to define regions. Because LWNet does not include optic disc segmentation weights and Automorph struggled with the disc segmentation of Rotterdam images (Table 2c), we used the same ground truth disc masks in both pipelines. The fovea location was also the same across models. Therefore, this comparison evaluates the effect of different models for artery-vein segmentation only.

Table 3 shows the results of the comparison, where we measured reduced mean absolute error and higher correlations when using VascX segmentations, across most features. Of 24 vascular features evaluated, 16 showed a significant improvement in MAE when compared to Automorph, and 22 when compared to LWNet. VascX also had the highest correlations with ground truth features in all but one case.

We report results of the same comparison on the Leuven-Haifa dataset (240 images with 30° FOV) in Table 5. These results show similar behavior. Although less features improved over Automorph in terms of MAE, all correlations favoured VascX.

Model	ChaseDB	DRHAGIS	HRF	RETA	FIVES	Leuven-Haifa	Rotterdam
Automorph	NA	.741	NA	NA	.824	.812	.810
LWNet	.732	.672	.573	NA	.756	.713	.745
VascX	.780	.769	.786	.890	.831	.829	.852

(a) Vessel segmentation (Dice score).

Model	HRF	-AV	RI	TE	Les	-AV	Leuve	n-Haifa	Rotte	erdam
	A	V	A	V	A	V	A	V	A	V
Automorph [57]	NA	NA	NA	NA	NA	NA	.707	.773	.712	.752
LWNet [19]	.506	.574	NA	NA	.618	.670	.569	.649	.635	.696
VascX	.746	.792	.711	.760	.800	.835	.786	.826	.817	.849

(b) Artery-vein segmentation (Dice score). A: arteries mask score, V: veins mask score

Model	ORIGA	PAPILA	IDRiD	ADAM	PALM	REFUGE2	Rotterdam
Automorph	.876	.618	.931	.958	.846	NA	.220
VascX	.958	.961	.958	.964	.921	.956	.886

(c) Disc segmentation (Dice score)

Model	IDRID	ADAM	PALM	REFUGE2	Rotterdam
VascX	14.68	11.15	26.22	10.68	25.14

⁽d) Fovea localization (L2/Euclidean distance to ground truth in pixels)

Table 2. Performance comparison of VascX segmentation models. *NA* is used for a model - dataset pair when the model was trained on the dataset and therefore it was not possible to benchmark this model - dataset pair on out-of-distribution data.

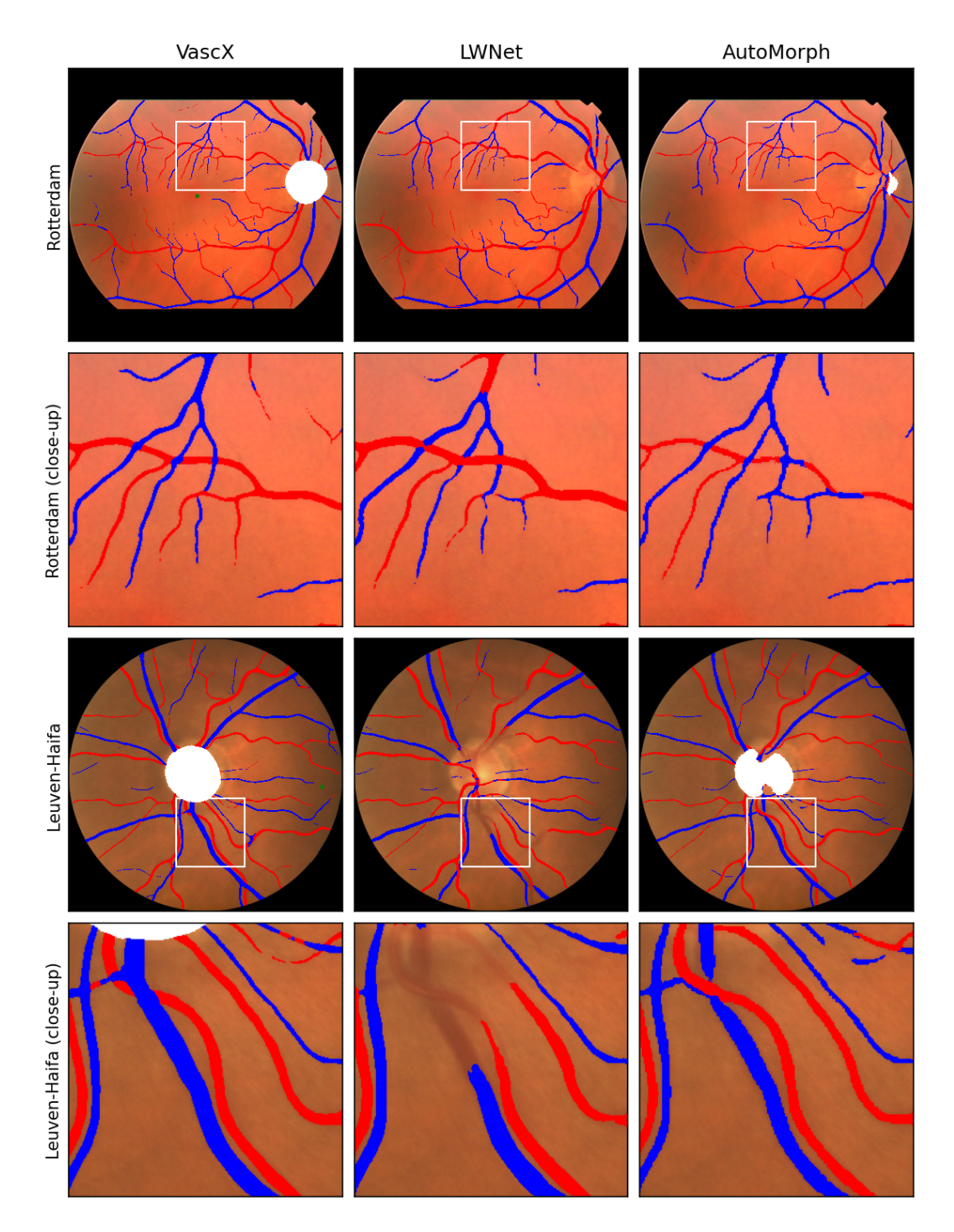


Figure 4. Example model outputs from the benchmarked systems showing A/V segmentation and disc and fovea outputs were applicable. We observed more consistency in A/V and disc segmentation from VascX. The CFIs shown correspond to the images with the median Dice score for A/V segmentation with VascX; for each dataset.

DISCUSSION

We presented new model ensembles for CFI vasculature analysis and benchmarked against publicly available systems. With the objective of developing models that operate robustly across devices and achieve performance improvements on the different imaging conditions found on real cohort studies and clinical datasets, we focused

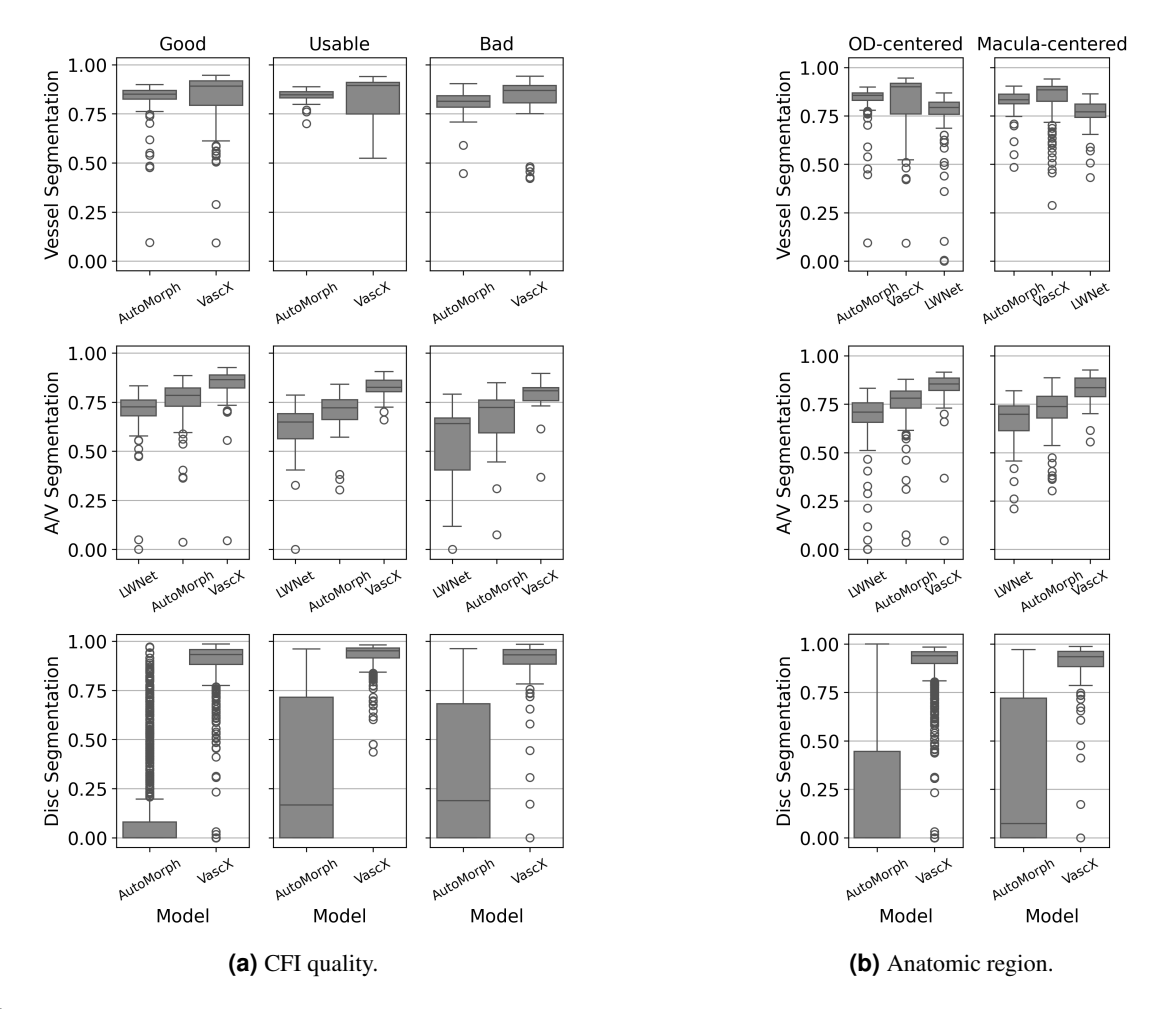


Figure 5. Box plots displaying the distribution of model performance (Dice score) over image quality and anatomic region (AR) bins/slices of the Rotterdam dataset. For vessel segmentation, the performance of the models is stable across quality and anatomic region bins. For artery-vein segmentation, the biggest improvement is in *usable* images. For disc segmentation, the model achieves remarkably stable performance across image quality and AR; while the images pose a challenge for Automorph.

on the diversity of our development set. We augmented more than 15 public datasets (each of which usually consist of carefully selected CFIs from one or a few devices) with CFIs collected in The Netherlands throughout more than three decades from 11 different imaging devices and with diverse pathology. Together, this resulted in a comprehensive set of images including a wider range of patient characteristics (origin, age, pathologies) and capture characteristics (device, anatomic region, field of view). For model training, we made use of well-known architectures, a new more robust pre-processing algorithm, and data augmentation to achieve solid performance across tasks.

Our main evaluation using Dice scores revealed consistently better performance from VascX when compared to existing publicly available models - Automorph and LWNET - across both public datasets and the Rotterdam sets. We observed an important improvement in A/V segmentation performance, crucial in vascular analysis pipelines. It stands out that the largest difference between VascX and the rest is in *usable* or intermediate quality images 5, common in large cohort studies and clinical data. A large improvement was observed in disc segmentation performance when compared to Automorph, which struggled with Rotterdam images likely due to its more limited training set [57]. Its performance was low for both disc and macula-centered images and across quality levels (5). A large difference was also observed in PAPILA 2, which has a 30 degree field of view not present in Automorph's training set. The differences in vessel segmentation performance were smaller between models, suggesting that performance in this task may already be saturated.

Our fovea localization model had mean L2 errors between 10.68 (REFUGE2) and 26.22 (PALM) on images

-							
	Gradar II		MAE		P	earson	r
	Grader μ	VascX	AM	LWN	VascX	AM	LWN
Temporal Angle - A	122.36	5.56	6.39*	8.63†	0.69	0.66	0.57
Temporal Angle - V	126.35	5.05	5.91	8.29†	0.77	0.73	0.65
CRE - A	10.53	0.93	1.49†	3.10†	0.79	0.57	0.49
CRE - V	15.83	1.11	1.94†	3.79†	0.82	0.70	0.51
Vasc. Density - A	4.25	0.33	0.85 †	$0.76 \dagger$	0.89	0.76	0.61
Vasc. Density - V	4.90	0.35	0.87†	1.12†	0.88	0.64	0.60
Vessel Caliber [med] - A	4.23	0.60	0.64	1.36†	0.63	0.48	0.37
Vessel Caliber [std] - A	2.26	0.27	0.39†	0.90 †	0.70	0.59	0.49
Vessel Caliber [med] - V	4.35	0.83	.72*	1.38†	0.49	0.54	0.38
Vessel Caliber [std]- V	3.15	0.26	0.47†	$0.79\dagger$	0.84	0.69	0.64
Tortuosity [med] - A	1.09	0.0058	0.006	0.0059	0.81	0.73	0.76
Tortuosity [med] - V	1.09	0.0048	0.0053	0.0059*	0.71	0.57	0.52
Curvature [med] - A	9.08	1.07	1.27*	1.34*	0.93	0.90	0.86
Curvature [med] - V	10.25	1.11	1.40†	1.44†	0.84	0.84	0.83
Inflection count [med] - A	1.46	0.48	0.61*	0.53	0.39	0.26	0.30
Inflection count [med] - V	1.57	0.45	0.50	0.60*	0.43	0.32	0.26
Tortuosity [LW] - A	1.12	0.017	0.019*	$0.038\dagger$	0.52	0.47	0.11
Tortuosity [LW] - V	1.11	0.012	0.014*	$0.033\dagger$	0.75	0.62	0.12
Bif. Angles [mean] - A	82.99	5.79	6.70*	9.51†	0.48	0.41	0.27
Bif. Angles [med] - A	81.83	5.19	6.15	8.97†	0.57	0.45	0.22
Bif. Angles [mean] - V	84.16	4.47	5.53*	7.71†	0.75	0.59	0.54
Bif. Angles [med] - V	83.20	3.75	5.02*	5.96†	0.74	0.52	0.56
Num. Bifurcations - A	27.32	10.34	10.97	12.59†	0.81	0.77	0.69
Num. Bifurcations - V	31.61	10.33	12.06†	13.48†	0.89	0.76	0.76

Table 3. Feature quality comparison on the Rotterdam sets (215 CFIs). Results of comparing MAE of features extracted using different models for artery-vein segmentation: VascX, Automorph (AM) and LittleWNet (LWN). Features extracted from ground truth segmentations were used as the reference for MAE. The feature implementation was the same across models. For vessel or bifurcation features, the aggregation function (applied on features from the whole image) is indicated in brackes: [med]: median, [std]: standard deviation, [mean]: mean value, [LW]: length-weighted; vessels were weighted by their length. Grader μ is the mean of feature values; mean MAE is the mean absolute error between ground truth features and features extracted from model outputs. Pearson coefficients are correlations between ground truth and model outputs. *: Significant difference in MAE (p < 0.05) between the model and VascX. †: p < 0.001

of $1024 \times 1024 px$. This model is enough to provide an approximate localization of the fovea center, useful for the automatic placement of retinal regions (eg. ETDRS grid) for localized measurements.

Importantly, our results showed that better segmentation performance translates into more accurate vascular features, in line with the results of Fhima et al. [15]. Features from VascX model segmentations show lower absolute error and higher correlation with features extracted directly from grader segmentations; when compared to features extracted from Automorph segmentations.

Further work is required in several areas. There is room for improvement in artery-vein segmentation, especially regarding the connectivity of the vessel trees. Despite the improvements, our model still produces A/V mis-classifications and gaps. Enforcing the expected tree structure in the segmentation is a notorious open challenge in deep learning. Incorporating specific loss functions [44] and post-processing steps [5] designed for connectivity may help address this issue.

The further development of retinal analysis pipelines and the development and evaluation of vascular features with clinical significance also holds promise. The feature computation stage involves significant nuance. Some features such as tortuosity, for example, may be particularly sensitive to discontinuities in the segmentation. The results in Table 3 support that some features are more robust than others to potential mistakes in the segmentations. Deeper evaluations of the robustness and predictive power of vascular features are in order. The ability to capture image quality for quality control and for informing feature computation may be crucial here. Classification

of image quality using a one-dimensional image-level label, while useful, is not granular enough for some applications. Artifacts may affect only part of the image. Defocus or poor overall quality may result in a CFI usable for analysis of the main vascular arches but not any smaller vessels. A decomposition of image quality into (localized) factors may be a necessary next step in developing more robust pipelines.

In summary, our results show that our models outperform those in previous systems in every dataset and condition we evaluated, likely due to the increased size and variety of our training set. We expect that VascX models will serve as the backbone for more robust CFI vascular analysis pipelines (and other CFI-based pipelines). To serve these goals, we have made available our entire inference pipeline, including model weights and inference code with a new CFI pre-processing algorithm. With this, we aim to catalyze research towards understanding how analysis of the retinal vasculature can help us prevent, detect and monitor diseases, not only of the eye but of the rest of the body.

ACKNOWLEDGMENTS

The authors acknowledge the staff of the Eyened Reading Center for their different roles in data collection and algorithm development. Special acknowledgment to the Sinergia consortium for conceiving and supporting this project. The authors are grateful to the study participants and the staff from the Rotterdam Study, AMD-Life; the Dutch Myopia Study and to all contributors to the (publicly available) datasets that we used to train our models. This work was funded by the Swiss National Science Foundation grant no. CRSII5_209510.

REFERENCES

- Or Abramovich, Hadas Pizem, Jan Van Eijgen, Ilan Oren, Joshua Melamed, Ingeborg Stalmans, Eytan Z. Blumenthal, and Joachim A. Behar. Fundusq-net: A regression quality assessment deep learning algorithm for fundus images quality grading. *Computer Methods and Programs in Biomedicine*, 239:107522, September 2023. ISSN 0169-2607. doi: 10.1016/j.cmpb.2023.107522. URL http://dx.doi.org/10.1016/j.cmpb.2023.107522.
- [2] Mansour Abtahi, David Le, Behrouz Ebrahimi, Albert Kofi Dadzie, Mojtaba Rahimi, Yi-Ting Hsieh, Michael J. Heiferman, Jennifer I. Lim, and Xincheng Yao. Quantitative artery-vein analysis in octa improves the performance of dr detection and classification. *Investigative Ophthalmology & Visual Science*, 65(9): PB0060, 2024.
- [3] Muhammad Naseer Bajwa, Gur Amrit Pal Singh, Wolfgang Neumeier, Muhammad Imran Malik, Andreas Dengel, and Sheraz Ahmed. G1020: A benchmark retinal fundus image dataset for computer-aided glaucoma detection, 2020.
- Attila Budai and Jan Odstrcilik. High resolution fundus (hrf) image database, 2013. URL https://www5.cs.fau.de/research/data/fundus-images/.
- [5] Sophie Carneiro-Esteves, Antoine Vacavant, and Odyssée Merveille. A plug-and-play framework for curvilinear structure segmentation based on a learned reconnecting regularization. *Neurocomputing*, 599: 128055, 2024. ISSN 0925-2312. doi: https://doi.org/10.1016/j.neucom.2024.128055. URL https://www.sciencedirect.com/science/article/pii/S0925231224008269.
- Wenting Chen, Shuang Yu, Kai Ma, Wei Ji, Cheng Bian, Chunyan Chu, Linlin Shen, and Yefeng Zheng. Tw-gan: Topology and width aware gan for retinal artery/vein classification. *Medical Image Analysis*, 77: 102340, 2022. ISSN 1361-8415. doi: https://doi.org/10.1016/j.media.2021.102340.
- [7] C Cheung and TY Wong. Quantitative and qualitative retinal microvascular characteristics and blood pressure. *Journal of Hypertension*, 29:1380–1391, 2011. doi: 10.1097/HJH.0b013e328347266c.
- [8] CYL Cheung, W Hsu, ML Lee, JJ Wang, P Mitchell, QP Lau, and TY Wong. A new method to measure peripheral retinal vascular caliber over an extended area. *Microcirculation*, 17:495–503, 2010. doi: 10.1111/j.1549-8719.2010.00048.x.
- [9] Alexandra P. M. de Koning-Backus, Jessica C. Kiefte-de Jong, Jeroen G. J. van Rooij, AMD-Life Team, André G. Uitterlinden, Trudy G. Voortman, Magda A. Meester-Smoor, and Caroline C. W. Klaver. Lifestyle intervention randomized controlled trial for age-related macular degeneration (amd-life): Study design.

- *Nutrients*, 15(3), 2023. ISSN 2072-6643. doi: 10.3390/nu15030602. URL https://www.mdpi.com/2072-6643/15/3/602.
- [10] N Dervenis, AL Coleman, A Harris, MR Wilson, F Yu, E Anastasopoulos, and F Topouzis. Factors associated with retinal vessel diameters in an elderly population: The thessaloniki eye study. *Investigative Ophthalmology & Visual Science*, 60:2208–2217, 2019. doi: 10.1167/iovs.18-26276.
- [11] Justin Engelmann, Diana Moukaddem, Lucas Gago, Niall Strang, and Miguel O. Bernabeu. Applicability of oculomics for individual risk prediction: Repeatability and robustness of retinal fractal dimension using dart and automorph. *Investigative Ophthalmology & Visual Science*, 65(6):10, 2024. doi: 10.1167/iovs.65.6.10.
- [12] H. Fang, F. Li, J. Wu, et al. Open fundus photograph dataset with pathologic myopia recognition and anatomical structure annotation. *Scientific Data*, 11:99, 2024. doi: 10.1038/s41597-024-02911-2.
- [13] Huihui Fang, Fei Li, Huazhu Fu, Xu Sun, Xingxing Cao, Fengbin Lin, Jaemin Son, Sunho Kim, Gwenole Quellec, Sarah Matta, Sharath M. Shankaranarayana, Yi-Ting Chen, Chuen-Heng Wang, Nisarg A. Shah, Chia-Yen Lee, Chih-Chung Hsu, Hai Xie, Baiying Lei, Ujjwal Baid, Shubham Innani, Kang Dang, Wenxiu Shi, Ravi Kamble, Nitin Singhal, Ching-Wei Wang, Shih-Chang Lo, Jose Ignacio Orlando, Hrvoje Bogunovic, Xiulan Zhang, and Yanwu Xu. Adam challenge: Detecting age-related macular degeneration from fundus images. IEEE Transactions on Medical Imaging, 41(10):2828–2847, October 2022. ISSN 1558-254X. doi: 10.1109/tmi.2022.3172773. URL http://dx.doi.org/10.1109/TMI.2022.3172773.
- [14] Huihui Fang, Fei Li, Junde Wu, Huazhu Fu, Xu Sun, Jaemin Son, Shuang Yu, Menglu Zhang, Chenglang Yuan, Cheng Bian, Baiying Lei, Benjian Zhao, Xinxing Xu, Shaohua Li, Francisco Fumero, José Sigut, Haidar Almubarak, Yakoub Bazi, Yuanhao Guo, Yating Zhou, Ujjwal Baid, Shubham Innani, Tianjiao Guo, Jie Yang, José Ignacio Orlando, Hrvoje Bogunović, Xiulan Zhang, and Yanwu Xu. Refuge2 challenge: A treasure trove for multi-dimension analysis and evaluation in glaucoma screening, 2022. URL https://arxiv.org/abs/2202.08994.
- [15] J. Fhima, J. Van Eijgen, M. I. Billen Moulin-Romsée, et al. Lunet: deep learning for the segmentation of arterioles and venules in high resolution fundus images. *Physiological Measurement*, 45(5):10.1088/1361–6579/ad3d28, 2024. doi: 10.1088/1361-6579/ad3d28. Published 2024 May 3.
- [16] Muhammad Moazam Fraz, Paolo Remagnino, Andreas Hoppe, Bunyarit Uyyanonvara, Alicja R. Rudnicka, Christopher G. Owen, and Sarah A. Barman. Chase db1: Retinal vessel reference dataset, 2012. URL https://researchdata.kingston.ac.uk/96/.
- [17] S Frost, Y Kanagasingam, SL Macaulay, et al. Retinal vascular biomarkers for early detection and monitoring of alzheimer's disease. *Translational Psychiatry*, 3:e233, 2013.
- [18] Huazhu Fu, Boyang Wang, Jianbing Shen, Shanshan Cui, Yanwu Xu, Jiang Liu, and Ling Shao. Evaluation of Retinal Image Quality Assessment Networks in Different Color-Spaces, page 48–56. Springer International Publishing, 2019. ISBN 9783030322397. doi: 10.1007/978-3-030-32239-7_6. URL http://dx.doi.org/10.1007/978-3-030-32239-7_6.
- [19] Adrian Galdran, André Anjos, José Dolz, Hadi Chakor, Hervé Lombaert, and Ismail Ben Ayed. The little w-net that could: State-of-the-art retinal vessel segmentation with minimalistic models, 2020.
- [20] Samuel David Gießer, Ferhat Turgut, Amr Saad, Chiara Sommer, Yukun Zhou, Siegfried Wagner, Pearse Andrew Keane, Matthias Becker, Delia Cabrera DeBuc, and Gabor Mark Somfai. A retest-stable vessel tortuosity metric for fundus photography. *Investigative Ophthalmology & Visual Science*, 65(7):2393, 2024.
- [21] Mariana Batista Gonçalves, Luis Filipe Nakayama, Daniel Ferraz, Hanna Faber, Edward Korot, Fernando Korn Malerbi, Caio Vinicius Regatieri, Mauricio Maia, Leo Anthony Celi, Pearse A Keane, et al. Image quality assessment of retinal fundus photographs for diabetic retinopathy in the machine learning era: A review. Eye, 38(3):426–433, 2024.
- [22] Annechien E. G. Haarman, Milly S. Tedja, Corina Brussee, Clair A. Enthoven, Gwyneth A. van Rijn, Johannes R. Vingerling, Jan E. E. Keunen, Camiel J. F. Boon, Annette J. M. Geerards, Gré P. M. Luyten, Virginie J. M. Verhoeven, and Caroline C. W. Klaver. Prevalence of Myopic Macular Features in Dutch

- Individuals of European Ancestry With High Myopia. *JAMA Ophthalmology*, 140(2):115–123, 02 2022. ISSN 2168-6165. doi: 10.1001/jamaophthalmol.2021.5346. URL https://doi.org/10.1001/jamaophthalmol.2021.5346.
- [23] S. Holm, G. Russell, V. Nourrit, and N. McLoughlin. Dr hagis a fundus image database for the automatic extraction of retinal surface vessels from diabetic patients. *J Med Imaging (Bellingham)*, 4(1):014503, Jan 2017. doi: 10.1117/1.JMI.4.1.014503. Epub 2017 Feb 9.
- [24] Yu Huang, Carol Y Cheung, Dawei Li, Yih Chung Tham, Bin Sheng, Ching Yu Cheng, Ya Xing Wang, and Tien Yin Wong. Ai-integrated ocular imaging for predicting cardiovascular disease: advancements and future outlook. *Eye*, 38(3):464–472, 2024.
- ^[25] LD Hubbard, RJ Brothers, WN King, et al. Methods for evaluation of retinal microvascular abnormalities associated with hypertension/sclerosis in the atherosclerosis risk in communities study. *Ophthalmology*, 106 (12):2269–2280, 1999.
- [26] M. A. Ikram, G. Brusselle, M. Ghanbari, et al. Objectives, design and main findings until 2020 from the rotterdam study. *European Journal of Epidemiology*, 35:483–517, 2020. doi: 10.1007/s10654-020-00640-5.
- [27] Fabian Isensee, Paul F Jaeger, Simon A Kohl, Jens Petersen, and Klaus H Maier-Hein. nnu-net: a self-configuring method for deep learning-based biomedical image segmentation. *Nature methods*, 18(2): 203–211, 2021.
- ^[28] A Iwase, A Sekine, J Suehiro, K Tanaka, Y Kawasaki, R Kawasaki, and M Araie. A new method of magnification correction for accurately measuring retinal vessel calibers from fundus photographs. *Investigative Ophthalmology & Visual Science*, 58:1858–1864, 2017. doi: 10.1167/iovs.16-21202.
- ^[29] K. Jin, X. Huang, J. Zhou, et al. Fives: A fundus image dataset for artificial intelligence based vessel segmentation. *Sci Data*, 9:475, 2022. doi: 10.1038/s41597-022-01564-3.
- [30] R Klein, CE Myers, MD Knudtson, KE Lee, R Gangnon, TY Wong, and BE Klein. Relationship of blood pressure and other factors to serial retinal arteriolar diameter measurements over time: The beaver dam eye study. *Archives of Ophthalmology*, 130:1019, 2012. doi: 10.1001/archophthalmol.2012.560.
- [31] O. Kovalyk, J. Morales-Sánchez, R. Verdú-Monedero, et al. Papila: Dataset with fundus images and clinical data of both eyes of the same patient for glaucoma assessment. *Sci Data*, 9:291, 2022. doi: 10.1038/s41597-022-01388-1.
- [32] Liangzhi Li, Manisha Verma, Yuta Nakashima, Hajime Nagahara, and Ryo Kawasaki. Iternet: Retinal image segmentation utilizing structural redundancy in vessel networks. In *The IEEE Winter Conference on Applications of Computer Vision (WACV)*, March 2020.
- [33] Bart Liefers, Jos Beekmans, Corina Brussee, Karin Alida van Garderen, Amal Hamimida, Annemiek Krijnen, Daniel Luttikhuizen, Magda A. Meester, Jose David Vargas Quiros, Jeroen Vermeulen, Irene van Zeijl, and Caroline C. W. Klaver. A vendor-independent platform for ai-assisted retinal image analysis. *Investigative Ophthalmology & Visual Science*, 65(7):5891, 2024.
- [34] G Liew, JJ Wang, P Mitchell, and TY Wong. Retinal vascular imaging: a new tool in microvascular disease research. *Circulation: Cardiovascular Imaging*, 1(2):156–161, 2008.
- [35] Ji Lin, Xingru Huang, Huiyu Zhou, Yaqi Wang, and Qianni Zhang. Stimulus-guided adaptive transformer network for retinal blood vessel segmentation in fundus images. *Medical Image Analysis*, 89:102929, 2023.
- [36] Xiang Lyu, Li Cheng, and Shuo Zhang. The reta benchmark for retinal vascular tree analysis. *Scientific Data*, 9:397, 2022. doi: 10.1038/s41597-022-01507-y.
- [37] José Ignacio Orlando, João Barbosa Breda, Karel van Keer, Matthew B. Blaschko, Pablo J. Blanco, and Carlos A. Bulant. Towards a glaucoma risk index based on simulated hemodynamics from fundus images. In Alejandro F. Frangi, Julia A. Schnabel, Christos Davatzikos, Carlos Alberola-López, and Gabor Fichtinger, editors, *Medical Image Computing and Computer Assisted Intervention MICCAI 2018*, pages 65–73, Cham, 2018. Springer International Publishing. ISBN 978-3-030-00934-2.

- [38] José Ignacio Orlando, Huazhu Fu, João Barbosa Breda, Karel van Keer, Deepti R. Bathula, Andrés Diaz-Pinto, Ruogu Fang, Pheng-Ann Heng, Jeyoung Kim, JoonHo Lee, Joonseok Lee, Xiaoxiao Li, Peng Liu, Shuai Lu, Balamurali Murugesan, Valery Naranjo, Sai Samarth R. Phaye, Sharath M. Shankaranarayana, Apoorva Sikka, Jaemin Son, Anton van den Hengel, Shujun Wang, Junyan Wu, Zifeng Wu, Guanghui Xu, Yongli Xu, Pengshuai Yin, Fei Li, Xiulan Zhang, Yanwu Xu, and Hrvoje Bogunović. Refuge challenge: A unified framework for evaluating automated methods for glaucoma assessment from fundus photographs. *Medical Image Analysis*, 59:101570, 2020. ISSN 1361-8415. doi: https://doi.org/10.1016/j.media.2019.101570. URL https://www.sciencedirect.com/science/article/pii/S1361841519301100.
- [39] Sofía Ortín Vela, Michael Johannes Beyeler, Olga Trofimova, Mattia Tomasoni, Ilaria Iuliani, David Presby, Florence Hoogewoud, and Sven Bergmann. Phenotypic and genetic characteristics of retinal vascular parameters and their association with diseases. *medRxiv*, 2023. doi: 10.1101/2023.07.07.23292368.
- [40] JC Parr and GF Spears. General caliber of the retinal arteries expressed as the equivalent width of the central retinal artery. *American Journal of Ophthalmology*, 77(4):472–477, 1974.
- [41] A Perez-Rovira, T MacGillivray, E Trucco, KS Chin, K Zutis, C Lupascu, and B Dhillon. Vampire: Vessel assessment and measurement platform for images of the retina. In 2011 Annual International Conference of the IEEE Engineering in Medicine and Biology Society, pages 3391–3394. IEEE, 2011. doi: 10.1109/IEMBS.2011.6090918.
- [42] Prasanna Porwal, Samiksha Pachade, Ravi Kamble, Manesh Kokare, Girish Deshmukh, Vivek Sahasrabuddhe, and Fabrice Meriaudeau. Indian diabetic retinopathy image dataset (idrid), 2018. URL https://dx.doi.org/10.21227/H25W98.
- [43] Touseef Ahmad Qureshi, Maged Habib, Andrew Hunter, and Bashir Al-Diri. A manually-labeled, artery/vein classified benchmark for the drive dataset. In *Proceedings of the 26th IEEE International Symposium on Computer-Based Medical Systems*, pages 485–488, 2013. doi: 10.1109/CBMS.2013.6627847.
- [44] Suprosanna Shit, Johannes C Paetzold, Anjany Sekuboyina, Ivan Ezhov, Alexander Unger, Andrey Zhylka, Josien PW Pluim, Ulrich Bauer, and Bjoern H Menze. cldice-a novel topology-preserving loss function for tubular structure segmentation. In *Proceedings of the IEEE/CVF Conference on Computer Vision and Pattern Recognition*, pages 16560–16569, 2021.
- [45] Gabor Mark Somfai, Samuel Giesser, Chiara Sommer, Matthias Becker, and Ferhat Turgut. The assessment of vessel segmentation reproducibility using automated retinal vascular morphology quantification (automorph). *Investigative Ophthalmology & Visual Science*, 64(9):PB0038, 2023.
- ^[46] Joes Staal, Michael D Abràmoff, Meindert Niemeijer, Max A Viergever, and Bram Van Ginneken. Ridgebased vessel segmentation in color images of the retina. *IEEE transactions on medical imaging*, 23(4): 501–509, 2004.
- [47] E Trucco, L Ballerini, D Relan, A Giachetti, T MacGillivray, K Zutis, and B Dhillon. Novel vampire algorithms for quantitative analysis of the retinal vasculature. In *Proceedings of the 2013 ISSNIP Biosignals and Biorobotics Conference: Biosignals and Robotics for Better and Safer Living (BRC)*, pages 1–4. IEEE, 2013. doi: 10.1109/BRC.2013.6487501.
- [48] E Trucco, A Giachetti, L Ballerini, D Relan, A Cavinato, and TJ MacGillivray. Morphometric measurements of the retinal vasculature in fundus images with vampire. In F Karray and A de Albuquerque Araujo, editors, *Biomedical Image Understanding: Methods and Applications*, pages 253–274. John Wiley & Sons, Hoboken, NJ, USA, 2015.
- [49] Jan Van Eijgen, Jonathan Fhima, Marie-Isaline Billen Moulin-Romsée, Joachim A. Behar, Eirini Christinaki, and Ingeborg Stalmans. Leuven-haifa high-resolution fundus image dataset for retinal blood vessel segmentation and glaucoma diagnosis. *Scientific Data*, 11(1):257, February 2024. ISSN 2052-4463. doi: 10.1038/s41597-024-03086-6. URL https://doi.org/10.1038/s41597-024-03086-6.

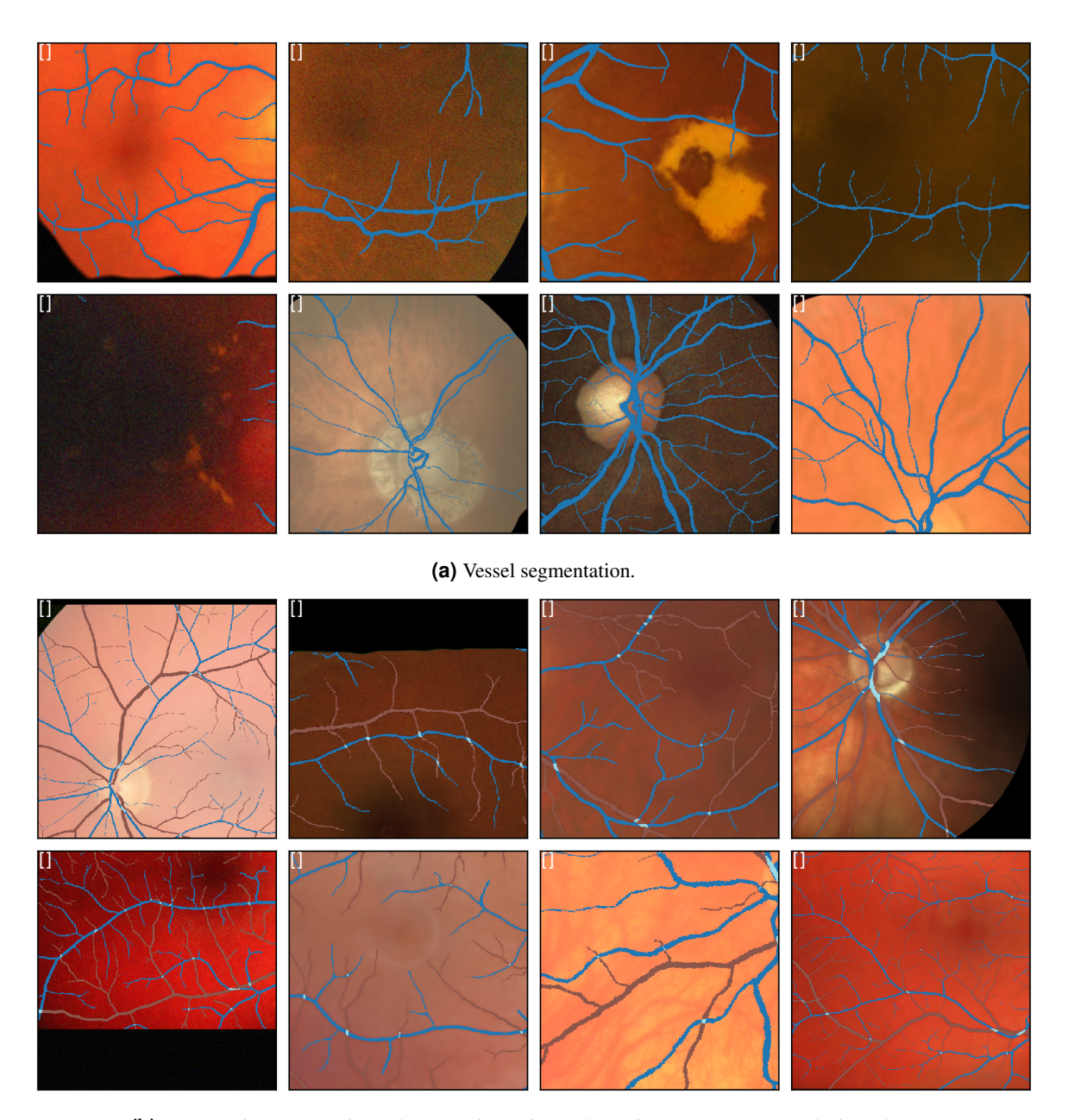
- [50] Siegfried K. Wagner, Mario Cortina-Borja, Steven M. Silverstein, Yukun Zhou, David Romero-Bascones, Robbert R. Struyven, Emanuele Trucco, Muthu R. K. Mookiah, Tom MacGillivray, Stephen Hogg, Timing Liu, Dominic J. Williamson, Nikolas Pontikos, Praveen J. Patel, Konstantinos Balaskas, Daniel C. Alexander, Kelsey V. Stuart, Anthony P. Khawaja, Alastair K. Denniston, Jugnoo S. Rahi, Axel Petzold, and Pearse A. Keane. Association Between Retinal Features From Multimodal Imaging and Schizophrenia. *JAMA Psychiatry*, 80(5):478–487, 05 2023. ISSN 2168-622X. doi: 10.1001/jamapsychiatry.2023.0171. URL https://doi.org/10.1001/jamapsychiatry.2023.0171.
- [51] Siegfried Karl Wagner, Vasiliki Bountziouka, Pirro Hysi, Jugnoo Sangeeta Rahi, Naomi Allen, Tariq Aslam, Denize Atan, Konstantinos Balaskas, Sarah Barman, Jenny Barrett, et al. Associations between unilateral amblyopia in childhood and cardiometabolic disorders in adult life: a cross-sectional and longitudinal analysis of the uk biobank. *EClinicalMedicine*, 70, 2024.
- [52] FF Wei, ZY Zhang, T Petit, N Cauwenberghs, YM Gu, L Thijs, and JA Staessen. Retinal microvascular diameter, a hypertension-related trait, in ecg-gated vs. non-gated images analyzed by ivan and siva. *Hypertension Research*, 39:886–892, 2016. doi: 10.1038/hr.2016.81.
- [53] TY Wong, R Klein, BEK Klein, et al. Retinal vessel diameters and their associations with age and blood pressure. *Investigative Ophthalmology & Visual Science*, 43(7):2859–2864, 2002.
- ^[54] TY Wong, FMA Islam, R Klein, BE Klein, MF Cotch, C Castro, and E Shahar. Retinal vascular caliber, cardiovascular risk factors, and inflammation: The multi-ethnic study of atherosclerosis (mesa). *Investigative Ophthalmology & Visual Science*, 47:2341–2350, 2006. doi: 10.1167/iovs.05-1539.
- ^[55] Tianhan Xu and Wataru Takano. Graph stacked hourglass networks for 3d human pose estimation. In *Proceedings of the IEEE/CVF conference on computer vision and pattern recognition*, pages 16105–16114, 2021.
- [56] Z. Zhang, F.S. Yin, J. Liu, W.K. Wong, N.M. Tan, B.H. Lee, J. Cheng, and T.Y. Wong. Origa(-light): an online retinal fundus image database for glaucoma analysis and research. In 2010 Annual International Conference of the IEEE Engineering in Medicine and Biology, pages 3065–3068. IEEE, 2010. doi: 10.1109/IEMBS.2010.5626137.
- Yukun Zhou, Siegfried K. Wagner, Mark A. Chia, An Zhao, Peter Woodward-Court, Moucheng Xu, Robbert Struyven, Daniel C. Alexander, and Pearse A. Keane. AutoMorph: Automated Retinal Vascular Morphology Quantification Via a Deep Learning Pipeline. *Translational Vision Science & Technology*, 11(7):12–12, 07 2022. ISSN 2164-2591. doi: 10.1167/tvst.11.7.12. URL https://doi.org/10.1167/tvst.11.7.12.

A DATASET DETAILS

Table 4. Complementary details of the public dataset used in model development. *: 379 of 1200 samples were discarded due to containing no disc segmentation for partially visible discs. †: 21 of 1200 CFIs were discarded due to having no associated annotation.

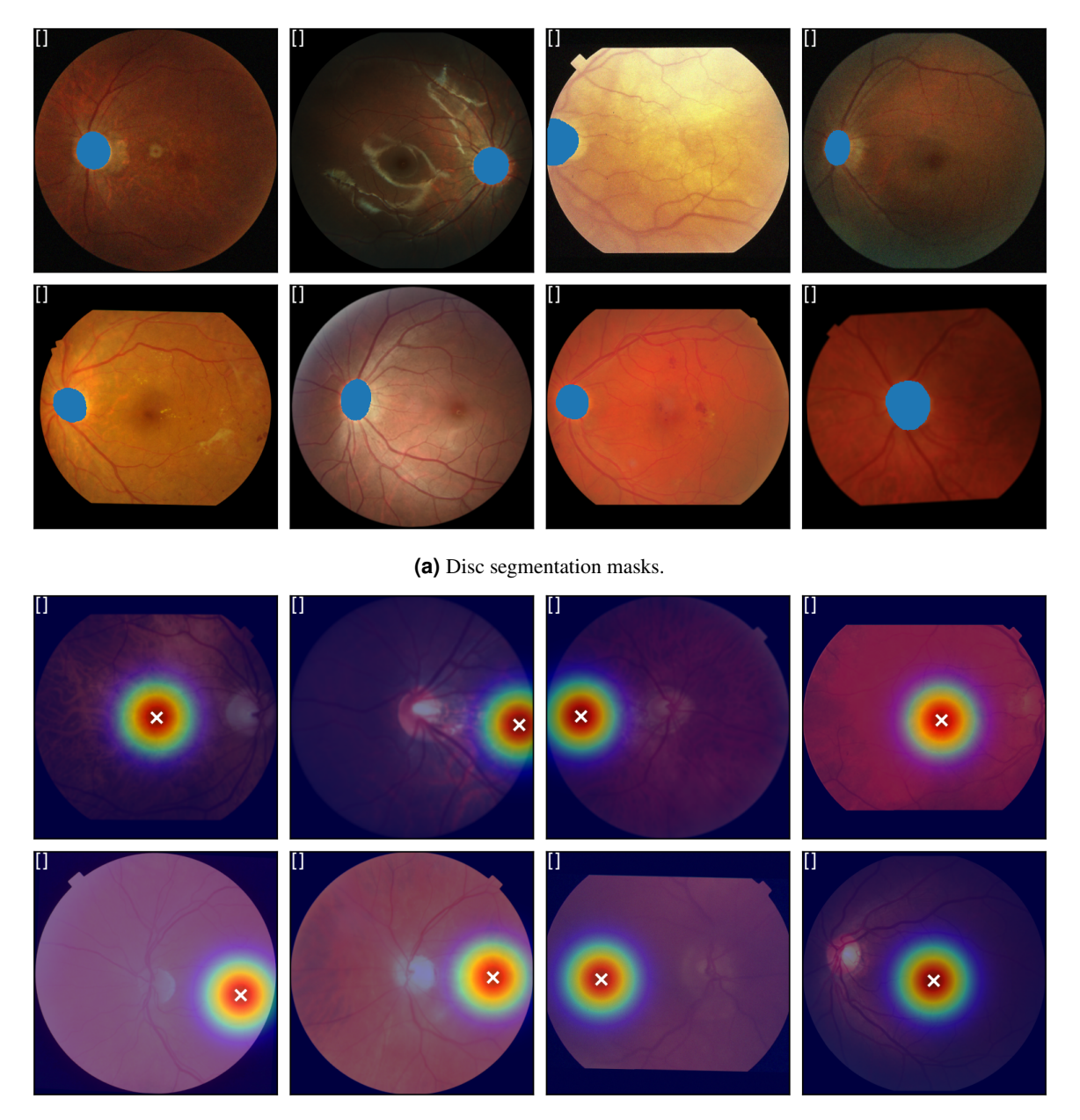
Dataset	N	Resolution	Devices
		Vessel Segmentation	
Chase DB [16]	28	35°, 1280 × 960	Nidek NM-200-D
DRHAGIS [23]	40	$45^{\circ}, 4752 \times 3168 - 2816 \times 1880$	Topcon TRC-NW6s, Topcon TRC-NW8, Canon CR DGi
HRF [4]	45	$45^{\circ}, 3504 \times 2336$	NR
RETA [36]	54	$50^{\circ}, 4288 \times 2848$	Kowa VX-10 alpha
FIVES [29]	800	$50^{\circ}, 2048 \times 2048$	Topcon TRC-NW8
Leuven-Haifa [49]	240	1444×1444	Zeiss Visucam 500
Rotterdam (ours)	352	see	Fig. 1
Total	1559		
		Artery Vein Segmentation	
RITE [43]	40	$45^{\circ},768\times584$	Canon CR5 3CCD
HRF-AV [6]	45	$45^{\circ}, 3504 \times 2336$	NR
Les-AV [37]	22	$30^{\circ}, 1444 \times 1620$	NR
Leuven-Haifa [49]	240	$30^{\circ}, 1444 \times 1444$	Zeiss Visucam 500
Rotterdam (ours)	215	see	Fig. 1
Total	562		
		Disc Segmentation	
ORIGA [56]	650	NR	NR
PAPILA [31]	488	45 $^{\circ}$, 2576 \times 1934	Topcon TRC-NW400
IDRiD [42]	81	$50^{\circ}, 4288 \times 2848$	Kowa VX-10 alpha
ADAM [13]	821*	2124×2056 , 1444×1444	Zeiss Visucam 500, Canon CR-2
PALM [12]	1179†	2124×2056 , 1444×1444	Zeiss Visucam 500, Canon CR-2
REFUGE2 [?]	2000	$1634 \times 1634 - 2124 \times 2056$	Zeiss Visucam 500, Canon CR
D. ((1 ()	1005		2, Topcon TRC-NW400, Kowa
Rotterdam (ours)	1225	see	Fig. 1
Total	7464		
		Fovea Localization	
IDRiD [42]	516	$50^{\circ}, 4288 \times 2848$	Kowa VX-10 alpha
ADAM [13]	1200	2124×2056 , 1444×1444	Zeiss Visucam 500, Canon CR-2
PALM [12]	1200	2124×2056 , 1444×1444	Zeiss Visucam 500, Canon CR-2
REFUGE2 [?]	2000	$1634 \times 1634 - 2124 \times 2056$	Zeiss Visucam 500, Canon CR 2, Topcon TRC-NW400, Kowa
Rotterdam (ours)	10908	see	Fig. 1
Total	15824		
		CFI Quality Estimation	
EyeQ [18]	28,792		

SAMPLE TRAINING BATCHES



(b) Artery-vein segmentation, where arteries, veins and crossings are separate (exclusive) classes.

Figure 6. Sample training batches of input images to vessel and artery-vein segmentation models after data augmentation, including the CFI and overlaid masks. The contrast enhanced image is not shown.



(b) Fovea localization heatmaps overlaid over the input images.

Figure 7. Sample training batches of input images to disc segmentation and fovea localization models after data augmentation. The contrast enhanced image is not shown.

B FEATURE COMPARISON

B.0.1 Feature implementations

In this section we describe the implementation of our vascular features, or refer to previous work for a detailed description.

Temporal Angle We followed the implementation presented in Ortín Vela et al. [39] (Section 2.3 of Supplementary Material).

CRE We followed the implementation presented in Ortín Vela et al. [39] (Section 2.2 of Supplementary Material). However, we measure and aggregate all vessels on the temporal side of the image that intersect the defined circle. We use only the temporal side because the nasal side is often not visible at the evaluated radii in fovea-centered images.

Vascular Density: Defined as the fraction of 1-pixels in the binary A/V segmentation mask within the fundus mask area:

$$\text{Vascular Density} = \frac{\sum_{i=1}^{H} \sum_{j=1}^{W} I(i,j) \cdot M(i,j)}{\sum_{i=1}^{H} \sum_{j=1}^{W} M(i,j)}$$

where:

- I(i, j) is the binary vessel mask where each pixel is either 0 (background) or 1 (vessel).
- M(i, j) is the binary mask where the region of interest (ROI) is defined, as extracted by our preprocessing algorithm

Vessel Caliber Vessel calibers or widths were measured per vessel segment by first fitting a spline to the segment skeleton. Perpendiculars to the spline were sampled at regular intervals. A ray casting method was used to extend the lines until they reached a background pixel (in the original artery or vein mask) on both sides, resulting in a width measurement. The median of the measurements was taken as the vessel segment caliber.

Tortuosity Tortuosity was defined using its common definition as the length of the vessel following its points divided by its chord length (distance between its endpoints):

$$T = \frac{\sum_{i=1}^{N-1} \sqrt{(x_{i+1} - x_i)^2 + (y_{i+1} - y_i)^2}}{\sqrt{(x_N - x_1)^2 + (y_N - y_1)^2}}$$

where (x_i, y_i) are the coordinates of the skeleton points, with i = 1, 2, ..., N where N is the total number of points along the vessel skeleton.

Curvature Curvature is an alternative measure of tortuosity. Given a parametrization $\gamma(t) = (x(t), y(t))$ of a twice differentiable plane curve, curvature can be expressed as:

$$\kappa = \frac{|x'y'' - y'x''|}{(x'^2 + y'^2)^{3/2}}$$

where the derivatives x', y', x'' and y'' are with respect to t.

The mean curvature over the curve can be defined by integration of this expression:

$$\bar{\kappa} = \int_0^1 \kappa(t)$$

This calculation was approximated by computing κ at regular intervals (every 5 pixels), using splines as parametrization to approximate derivatives.

Inflection count Another alternative measure of tortuosity, this feature counts the number of inflection points (changes of direction) in a vessel segment.

Num. Bifurcations The number of bifurcations detected in the image. Bifurcations are detected by converting the skeleton into a graph, which is then traversed using the optic disc location as reference to defined outgoing vessels.

Bif. Angles Smallest angle between the two child vessels in a bifurcation. A distance δ from the bifurcation point was defined, at which the angle is measured. The spline approximations are used to obtain points (x,y) along the vessel segments at such δ . Bifurcations with child vessels shorter than δ are ignored.

	G 1		MAE		Pearson r			
	Grader μ	VascX	AM	LWN	VascX	AM	LWN	
Temporal Angle - A	127.49	3.44	5.40†	10.48†	0.81	0.72	0.56	
Temporal Angle - V	132.46	3.02	4.85	11.68†	0.86	0.74	0.39	
CRE - A	12.28	1.81	1.98	2.98†	0.68	0.38	0.22	
CRE - V	19.98	1.98	2.80†	4.70†	0.74	0.58	0.14	
Vasc. Density - A	4.76	0.58	1.15†	1.42†	0.77	0.61	0.48	
Vasc. Density - V	5.43	0.58	1.01†	1.31†	0.79	0.63	0.39	
Vessel Caliber [med] - A	5.25	1.37	1.33	1.73†	0.20	0.18	0.09	
Vessel Caliber [std] - A	3.06	0.43	0.65†	0.65†	0.73	0.57	0.47	
Vessel Caliber [med] - V	5.36	1.50	1.58	2.24†	0.45	0.36	0.15	
Vessel Caliber [std] - V	4.81	0.49	0.89 †	$0.74 \dagger$	0.76	0.67	0.36	
Tortuosity [med] - A	1.09	0.0057	0.0064	0.008 †	0.82	0.78	0.71	
Tortuosity [med] - V	1.08	0.0044	0.0046	0.0064†	0.77	0.76	0.51	
Curvature [med] - A	6.71	1.01	1.10	1.37†	0.91	0.90	0.85	
Curvature [med] - V	7.83	1.19	1.31	1.34	0.81	0.77	0.76	
Inflection count [med] - A	1.69	0.51	0.56	0.69†	0.38	0.19	0.22	
Inflection count [med] - V	1.85	0.62	0.71	0.76*	0.35	0.16	0.19	
Tortuosity [LW] - A	1.12	0.023	0.027†	$0.06 \dagger$	0.17	0.15	-0.29	
Tortuosity [LW] - V	1.11	0.019	0.021†	$0.054\dagger$	0.25	0.24	0.02	
Bif. Angles [mean] - A	79.88	7.69	7.11	11.58†	0.61	0.57	0.35	
Bif. Angles [med] - A	78.46	7.83	7.24*	10.75*	0.61	0.53	0.38	
Bif. Angles [mean] - V	81.36	7.21	6.76	10.63†	0.44	0.40	0.22	
Bif. Angles [med] - V	81.55	6.77	6.56	9.51†	0.50	0.42	0.26	
Num. Bifurcations - A	15.97	6.43	6.84*	7.62†	0.70	0.70	0.68	
Num. Bifurcations - V	18.11	7.79	7.64	9.11†	0.76	0.71	0.61	

Table 5. Feature quality comparison on the Leuven-Haifa dataset (240 CFIs). Results of comparing MAE of features extracted using different models for artery-vein segmentation: VascX, Automorph (AM) and LittleWNet (LWN). Features extracted from ground truth segmentations were used as the reference for MAE. For vessel or bifurcation features, the aggregation function (applied on features from the whole image) is indicated in brackes: [med]: median, [std]: standard deviation, [mean]: mean value, [LW]: length-weighted; vessels were weighted by their length. The feature implementation was the same across models. Grader μ is the mean of feature values; mean MAE is the mean absolute error between ground truth features and features extracted from model outputs. Pearson coefficients are correlations between ground truth and model outputs. *: Significant difference in MAE (p < 0.05) between the model and VascX. †: p < 0.001